Supporting Information for "Towards understanding polar heat transport enhancement in sub-glacial oceans on icy moons"

Robert Hartmann[1], Richard J.A.M. Stevens[1], Detlef Lohse[1,2], and Roberto Verzicco[1,3,4]

[1]Physics of Fluids Group and Twente Max Planck Center, J.M. Burgers Center for Fluid Dynamics, University of Twente, 7500 AE Enschede, The Netherlands

[2]Max Planck Institute for Dynamics and Self-Organisation, 37077 Göttingen, Germany

[3]Dipartimento di Ingegneria Industriale, University of Rome 'Tor Vergata', 00133 Rome, Italy

[4]Gran Sasso Science Institute, 67100 L'Aquila, Italy

Contents of this file

Introduction

Further details of the direct numerical simulations (DNSs) of rotating Rayleigh-Bénard convection (RRBC) in the spherical geometry (controlled by the dimensionless Prandtl number Pr, Rayleigh number Ra, and Rossby (or Ekman) number Ro (Ek), see main letter for full definitions) are provided in this file.

Text S1: Numerical Details

The DNSs use a central second-order accurate finite-difference scheme on a staggered grid in spherical coordinates (Santelli et al., 2020). The code, specialized for Rayleigh-Bénard systems, has been adopted to account for constant rotation around its central polar axis in the limit of a rotational Froude number $Fr = 0$, i.e., accounting for Coriolis forcing but neglecting the effect of centrifugal forcing on buoyancy (Wang et al., 2021). The limit of $Fr \to 0$ is valid in most geo- and astrophysical contexts (e.g., $Fr_{\text{Earth}} \approx 8.7 \cdot 10^{-5}$). All DNSs simulate a full spherical shell, i.e., no symmetric folding is applied along the Longitude ϑ, to not affect the dynamics across the polar axis in the buoyancy-dominated and rotation-affected regimes by enforcing a fully symmetric behavior around the polar axis.

All DNSs are performed at $Ra = 10^6$. The number of grid points in radial direction varies between $N_r = 72$ for constant $g(r) = g_0$ and $N_r = 108$ for $g(r) \propto r^{-2}$. A clipped Chebyshev-like clustering of grid points towards the plates is applied in the radial direction to ensure a sufficient resolution of the plate boundary layers. The resolution of the thermal/kinetic boundary layers strictly follows (Shishkina et al., 2010):

$$N_{BL,\Theta} \gtrsim 0.47 \cdot \sqrt{2 \cdot Nu_{\text{est}}} \tag{1}$$

$$N_{BL,u} \gtrsim 0.48 \cdot \sqrt{2 \cdot Nu_{\text{est}}} \cdot Pr^{1/3} \tag{2}$$

Here, $N_{BL,\{\Theta,u\}}$ is the number of grid points in the boundary layer and Nu_{est} a *a priori* estimate of the Nusselt number. The spatial directions are uniformly spaced in angle φ and ϑ, accounting for their maximal spacing at equator of the outer sphere. The dynamic

time stepping in our DNSs is controlled by a maximum CFL number (1.1) and a maximum time step ($5 \cdot 10^{-3}$ free-fall time units). The numerical parameters of the DNSs are summarized Tabs. S1-S3. All DNSs are run very long such that integral flow properties (like the Nusselt number Nu) are converged within a tolerance of 0.5%.

Text S2: Heat transport scaling at rapid rotation

The heat transport in rapidly rotating Rayleigh-Bénard convection (with $Ek \to 0$) is found to scale with the supercriticality of the system (King et al., 2012; Julien et al., 2012; Stellmach et al., 2014; Cheng et al., 2015):

$$Nu \propto \left(Ra\, Ek^{4/3}\right)^{\alpha} \tag{3}$$

In the canonical RRBC in planar configuration with no-slip boundaries, $\alpha = 3$ is predicted for $Ra \lesssim Ek^{-3/2}$ (King et al., 2012, 2013). On the contrary, $\alpha = 3/2$ is predicted in the asymptotic limit without molecular diffusion, which is known as *diffusion-free scaling*. Diffusion-free scaling in planar RRBC is only found for free-slip boundary conditions and small $Ek \lesssim 10^{-6}$ (Stellmach et al., 2014; Kunnen et al., 2016; Wang et al., 2021) or in asymptotically reduced models (Julien et al., 2012). The difference between $\alpha = 3$ and $\alpha = 3/2$ is attributed to the active role of Ekman pumping for no-slip boundaries (Stellmach et al., 2014; Julien et al., 2016; Plumley et al., 2016).

However, both scaling types are reported for spherical RRBC. Inside the polar tangent cylinder, i.e, the cylinder aligned with the polar axis and radius r_i of the inner sphere, an exponent $\alpha = 3$ is found (Wang et al., 2021; Gastine & Aurnou, 2023), whereas $\alpha = 3/2$

is observed at low latitudes outside the tangent cylinder (Gastine et al., 2016; Wang et al., 2021).

From Eq. 4 follows that, for fixed Pr and Ra, the heat transport in the rotation-dominated regime (if approaching the quasi-geostrophic state) should follow:

$$Nu \propto Ro^{\frac{4}{3}\alpha} = \begin{cases} Ro^4 & : \alpha = 3 \\ Ro^2 & : \alpha = 3/2 \end{cases} \tag{4}$$

Although our simulations do not reach to small $Ek < 10^{-6}$, we observe considerable different scaling behavior for the heat transport inside and outside the tangent cylinder, which almost meet the scaling exponents 4 and 2 predicted by Eq. 4 (see Fig. S4).

Text S3: Influence of the gravity profile on the effective Rayleigh number

The definition of the classical Rayleigh number Ra does only account for a constant gravitational acceleration g_0. Whenever the actual gravitational acceleration g varies locally, the effective Rayleigh number Ra_{eff}, i.e., the volume averaged local Rayleigh number of the system, differs from Ra. In our case the reference Ra is defined as:

$$Ra = \frac{\alpha g_0 \Delta T H^3}{\nu \kappa} \ , \tag{5}$$

where g_0 is the reference gravitational acceleration at the outer sphere (ν, κ, α, ΔT, and H are the kinematic viscosity, the thermal diffusivity, the isobaric thermal expansion coefficient, the temperature difference between inner and outer sphere, and the shell thickness, respectively). For any gravity profile $g(r) = g_0 \, (r/r_o)^\gamma$ with $\gamma \neq 0$, the effective Rayleigh

number changes depending on γ:

$$Ra_{\text{eff}} \equiv \left\langle \frac{\alpha g(r) \Delta T H^3}{\nu \kappa} \right\rangle_V = Ra \left\langle \left(\frac{r}{r_o} \right)^\gamma \right\rangle_V = Ra \, \frac{3}{(r_o^3 - r_i^3)} \int_{r_i}^{r_o} \left(\frac{r}{r_o} \right)^\gamma r^2 \mathrm{d}r \ , \quad (6)$$

where r_i and r_o are the radii of inner and outer sphere and $\langle \cdot \rangle_V$ denotes the volume average over the full shell. Solving the integral for $\gamma = 1$, 0, and -2 and $\eta = r_i/r_o = 0.6$ yields:

$$Ra_{\text{eff}} = \begin{cases} Ra \, \frac{3\eta}{1+\eta+\eta^2+\eta^3} \approx 0.83 \, Ra & : \gamma = 1 \\ Ra & : \gamma = 0 \\ Ra \, \frac{3}{1+\eta+\eta^2} \approx 1.53 \, Ra & : \gamma = -2 \end{cases} \quad (7)$$

Considering Ra_{eff} in the estimates for the optimal rotation rate $Ro_{\text{opt}}^{-1} \propto Ra_{\text{eff}}^{1/6}$ and the onset of convection $Ro_c^{-1} \propto Ra_{\text{eff}}^{1/4}$ then yields

$$Ro_{\text{opt},\gamma}^{-1} \approx \begin{cases} 0.83^{1/6} \, Ro_{\text{opt},\gamma=0}^{-1} \approx 0.97 \, Ro_{\text{opt},\gamma=0}^{-1} & : \gamma = 1 \\ 1.53^{1/6} \, Ro_{\text{opt},\gamma=0}^{-1} \approx 1.07 \, Ro_{\text{opt},\gamma=0}^{-1} & : \gamma = -2 \end{cases} \quad (8)$$

and

$$Ro_{c,\gamma}^{-1} \approx \begin{cases} 0.83^{1/4} \, Ro_{c,\gamma=0}^{-1} \approx 0.95 \, Ro_{c,\gamma=0}^{-1} & : \gamma = 1 \\ 1.53^{1/4} \, Ro_{c,\gamma=0}^{-1} \approx 1.11 \, Ro_{c,\gamma=0}^{-1} & : \gamma = -2 \end{cases} \quad (9)$$

This can help to explain the observed minimal trend in the shift of Ro_{opt}^{-1} (and likewise Ro_c^{-1}) in the tangent cylinder for the different γ (main letter Fig. 3).

References

Cheng, J. S., Stellmach, S., Ribeiro, A., Grannan, A., King, E. M., & Aurnou, J. M. (2015). Laboratory-numerical models of rapidly rotating convection in planetary cores. *Geophys. J. Int.*, *201*, 1–17.

Gastine, T., & Aurnou, J. M. (2023). Latitudinal regionalization of rotating spherical shell convection. *J. Fluid Mech.*, *954*, R1.

Gastine, T., Wicht, J., & Aubert, J. (2016). Scaling regimes in spherical shell rotating convection. *J. Fluid Mech.*, *808*, 690–732.

Julien, K., Aurnou, J. M., Calkins, M. A., Knobloch, E., Marti, P., Stellmach, S., & Vasil, G. M. (2016). A nonlinear model for rotationally constrained convection with Ekman pumping. *J. Fluid Mech.*, *798*, 50–87.

Julien, K., Knobloch, E., Rubio, A. M., & Vasil, G. M. (2012). Heat transport in low-Rossby-number Rayleigh-Bénard convection. *Phys. Rev. Lett.*, *109*(25), 254503.

King, E. M., Stellmach, S., & Aurnou, J. M. (2012). Heat transfer by rapidly rotating Rayleigh-Bénard convection. *J. Fluid Mech.*, *691*, 568–582.

King, E. M., Stellmach, S., & Buffett, B. (2013). Scaling behaviour in Rayleigh-Bénard convection with and without rotation. *J. Fluid Mech.*, *717*, 449–471.

Kunnen, R. P. J., Ostilla-Mónico, R., Poel, E. P. v. d., Verzicco, R., & Lohse, D. (2016). Transition to geostrophic convection: The role of the boundary conditions. *J. Fluid Mech.*, *799*, 413–432.

Plumley, M., Julien, K., Marti, P., & Stellmach, S. (2016). The effects of Ekman pumping on quasi-geostrophic Rayleigh-Bénard convection. *J. Fluid Mech.*, *803*, 51–71.

Santelli, L., Orlandi, P., & Verzicco, R. (2020). A finite-difference scheme for three-dimensional incompressible flows in spherical coordinates. *J. Comput. Phys.*, *424*, 109848.

Shishkina, O., Stevens, R. J. A. M., Grossmann, S., & Lohse, D. (2010). Boundary layer structure in turbulent thermal convection and its consequences for the required numerical resolution. *New J. Phys.*, *12*, 075022.

Stellmach, S., Lischper, M., Julien, K., Vasil, G., Cheng, J. S., Ribeiro, A., ... Aurnou, J. M. (2014). Approaching the Asymptotic Regime of Rapidly Rotating Convection:

Boundary Layers versus Interior Dynamics. *Phys. Rev. Lett.*, *113*, 254501.

Wang, G., Santelli, L., Lohse, D., Verzicco, R., & Stevens, R. J. A. M. (2021). Diffusion-free scaling in rotating spherical Rayleigh-Bénard convection. *Geophys. Res. Lett.*, *48*(20), e2021GL095017.

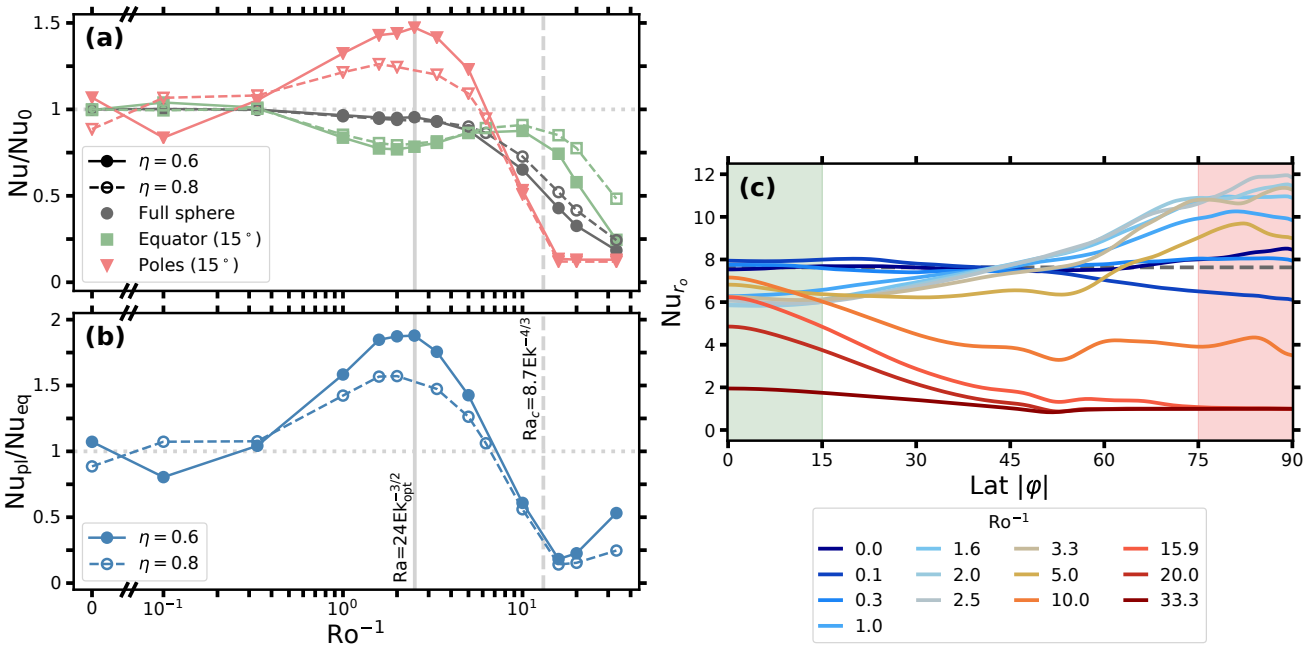

Figure S1. **(a)** Heat transport Nu relative to the non-rotating reference Nu_0 as a function of Ro^{-1} for different η with constant $g(r) = g_0$, $Pr = 4.38$, $Ra = 10^6$ averaged over the full sphere ($Nu \equiv \langle Nu_{r_o} \rangle_\varphi$), in 15° around the pole ($Nu_{\mathrm{pl}} = \langle Nu_{r_o} \rangle_{|\varphi|>75°}$), and in 15° around the equator ($Nu_{\mathrm{eq}} = \langle Nu_{r_o} \rangle_{|\varphi|<15°}$). **(b)** Ratio between the polar heat transport Nu_{pl} and the equatorial heat transport Nu_{eq} as a function of Ro^{-1}. **(c)** Dimensionless heat transport at the outer sphere Nu_{r_o} as function of the latitude $|\varphi|$ for various rotation rates Ro^{-1} with $Ra = 10^6$, $Pr = 4.38$, $\eta = 0.6$ and $g(r) = g_0$, where the color shaded regions illustrate the limited averaging.

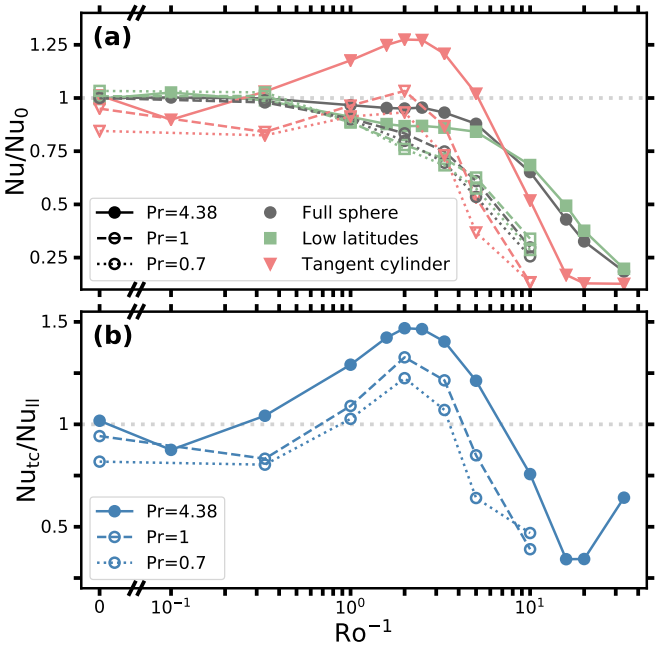

Figure S2. **(a)** Heat transport Nu relative to the non-rotating reference Nu_0 for the full sphere ($Nu \equiv \langle Nu_{r_o} \rangle_\varphi$), in the polar region ($Nu_{\rm tc} = \langle Nu_{r_o} \rangle_{|\varphi|>|\varphi_{\rm tc}|}$), and in the complementary low latitude region ($Nu_{\rm ll} = \langle Nu_{r_o} \rangle_{|\varphi|<|\varphi_{\rm tc}|}$), and **(b)** ratio between the heat transport in the polar region $Nu_{\rm tc}$ and the low latitude region $Nu_{\rm ll}$ as a functions of Ro^{-1} for different Pr with constant $g(r) = g_0$, $\eta = 0.6$, $Ra = 10^6$.

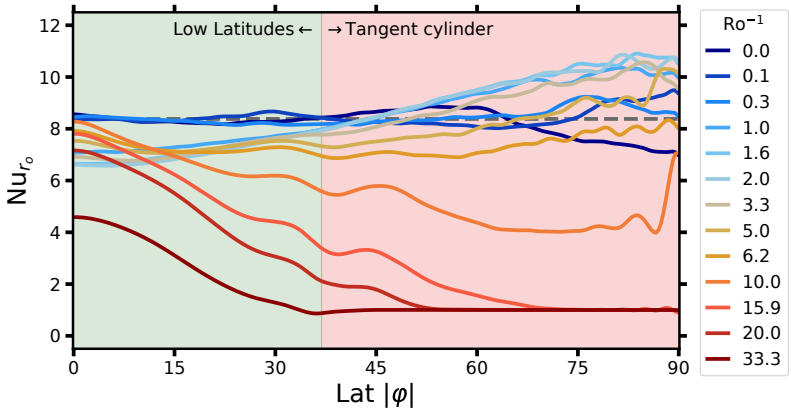

Figure S3. Dimensionless heat transport at the outer sphere Nu_{r_o} as function of the latitude $|\varphi|$ for various rotation rates Ro^{-1} at $Ra = 10^6$ and $Pr = 4.38$ with $\eta = 0.8$ and constant $g(r) = g_0$.

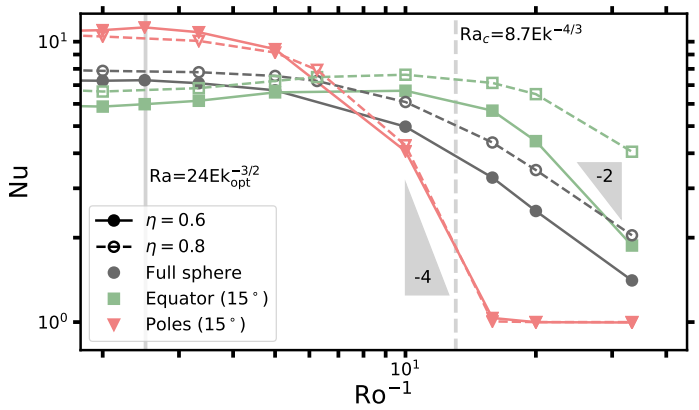

Figure S4. Heat transport Nu as a function of Ro^{-1} for $\eta = 0.6$ and 0.8 with constant $g(r) = g_0$, $Pr = 4.38$, $Ra = 10^6$ averaged over the full sphere, in 15° around the pole, and in 15° around the equator. Zoomed view on the rotation-dominated regime and the onset of convection highlighting the different effective scalings of the heat transport inside and outside the polar tangent cylinder.

Table S1. Summary of numerical parameters for the DNSs, all at $Pr = 4.38$ and $Ra = 10^6$, for $\gamma = 0$: radius ratio η; gravity exponent γ; inverse Rossby number Ro^{-1}; number of grid points in radial, latitudinal and longitudinal directions N_r, N_φ, N_ϑ; averaging interval $\Delta t_{\rm avg}$ in units of free-fall time; Nusselt number Nu averaged over the entire $\delta t_{\rm avg}$; Nusselt number Nu_h averaged over the 2nd half of $\delta t_{\rm avg}$; Nusselt number inside and outside the polar tangent cylinder $Nu_{\rm tc}$ and $Nu_{\rm ll}$, respectively.

η	γ	Ro^{-1}	N_r	N_φ	N_ϑ	$\Delta t_{\rm avg}$	Nu	Nu_h	$Nu_{\rm tc}$	$Nu_{\rm ll}$
0.6	0	0	72	384	768	900	7.634	7.633	7.729	7.596
0.6	0	0.1	72	384	768	900	7.651	7.643	6.856	7.831
0.6	0	$0.\bar{3}$	72	384	768	900	7.620	7.617	7.864	7.548
0.6	0	1	72	384	768	889	7.376	7.377	8.983	6.958
0.6	0	1.6	72	384	768	900	7.276	7.274	9.534	6.699
0.6	0	2	72	384	768	900	7.275	7.259	9.731	6.624
0.6	0	2.5	80	384	768	900	7.289	7.289	9.716	6.633
0.6	0	$3.\bar{3}$	72	384	768	900	7.110	7.116	9.222	6.569
0.6	0	5	72	384	768	900	6.709	6.715	7.789	6.423
0.6	0	10	72	384	768	900	4.977	4.960	3.959	5.228
0.6	0	15.9	72	384	768	900	3.275	3.282	1.289	3.770
0.6	0	20	72	384	768	900	2.490	2.480	0.984	2.872
0.6	0	$33.\bar{3}$	72	384	768	900	1.408	1.407	0.968	1.508
0.8	0	0	72	512	1024	500	8.380	8.376	8.458	8.316
0.8	0	0.1	72	512	1024	500	8.371	8.385	8.276	8.422
0.8	0	$0.\bar{3}$	72	512	1024	496	8.355	8.358	8.434	8.294
0.8	0	1	72	512	1024	500	8.047	8.044	9.003	7.401
0.8	0	1.6	72	512	1024	500	7.927	7.922	9.127	7.121
0.8	0	2	72	512	1024	500	7.870	7.863	9.101	7.041
0.8	0	$3.\bar{3}$	72	512	1024	500	7.784	7.786	8.700	7.165
0.8	0	5	72	512	1024	500	7.550	7.554	7.905	7.301
0.8	0	6.25	72	512	1024	597	7.240	7.239	7.155	7.292
0.8	0	10	72	512	1024	500	6.093	6.100	4.931	6.863
0.8	0	15.9	72	512	1024	900	4.370	4.369	2.187	5.815
0.8	0	20	72	512	1024	900	3.485	3.475	1.338	4.912
0.8	0	$33.\bar{3}$	72	512	1024	900	2.040	2.042	0.989	2.743

Table S2. Summary of numerical parameters for the DNSs, all at $Pr = 4.38$ and $Ra = 10^6$, for $\gamma \neq 0$ (columns as in Tab. S1).

η	γ	Ro^{-1}	N_r	N_φ	N_ϑ	Δt_{avg}	Nu	Nu_h	Nu_{tc}	Nu_{ll}
0.6	1	0	80	384	768	600	6.988	6.981	6.423	7.103
0.6	1	0.1	80	384	768	600	7.001	7.007	6.416	7.113
0.6	1	$0.\bar{3}$	80	384	768	600	6.961	6.952	7.342	6.833
0.6	1	1	80	384	768	600	6.745	6.744	8.515	6.269
0.6	1	2	80	384	768	600	6.637	6.642	8.883	6.040
0.6	1	2.5	80	384	768	600	6.578	6.571	8.653	6.027
0.6	1	$3.\bar{3}$	80	384	768	597	6.450	6.436	8.070	6.010
0.6	1	5	80	384	768	1000	5.921	5.929	6.555	5.734
0.6	1	10	80	384	768	1000	4.124	4.131	2.817	4.430
0.6	1	20	80	384	768	985	2.040	2.042	0.951	2.361
0.6	-2	0	108	432	864	489	9.318	9.320	8.256	9.559
0.6	-2	$0.\bar{3}$	108	432	864	592	9.253	9.240	8.996	9.291
0.6	-2	1	108	432	864	591	8.984	8.998	10.475	8.589
0.6	-2	2	108	432	864	554	8.799	8.784	11.749	8.044
0.6	-2	$3.\bar{3}$	108	432	864	578	8.737	8.747	11.723	7.976
0.6	-2	5	108	432	864	535	8.538	8.548	10.948	7.918
0.6	-2	10	108	432	864	756	7.170	7.159	7.379	7.101
0.6	-2	20	108	432	864	1047	4.346	4.356	2.469	4.791

Table S3. Summary of numerical parameters for the DNSs for $Pr \neq 4.38$, $Ra = 10^6$, $\eta = 0.6$, $\gamma = 0$ (columns as in Tab. S1 with Pr instead of η and γ).

Pr	Ro^{-1}	N_r	N_φ	N_ϑ	Δt_{avg}	Nu	Nu_h	Nu_{tc}	Nu_{ll}
1	0	72	384	768	665	7.507	7.507	7.132	7.566
1	$0.\bar{3}$	72	384	768	377	7.352	7.333	6.308	7.580
1	1	72	384	768	600	6.786	6.810	7.238	6.641
1	2	72	384	768	600	6.259	6.256	7.758	5.846
1	$3.\bar{3}$	72	384	768	600	5.611	5.611	6.517	5.365
1	5	72	384	768	600	4.576	4.571	3.990	4.701
1	10	72	384	768	1000	2.237	2.233	0.993	2.544
0.7	0	72	384	768	114	7.335	7.34	6.200	7.579
0.7	$0.\bar{3}$	72	384	768	286	7.256	7.242	6.046	7.528
0.7	1	72	384	768	600	6.582	6.578	6.697	6.523
0.7	2	72	384	768	600	5.857	5.855	6.838	5.581
0.7	$3.\bar{3}$	72	384	768	600	5.104	5.107	5.365	5.014
0.7	5	72	384	768	1000	3.925	3.934	2.699	4.215
0.7	10	72	384	768	1000	1.876	1.876	0.984	2.096